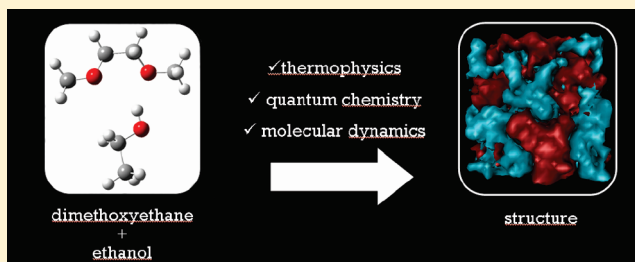


## Study of Dimethoxyethane/Ethanol Solutions

Santiago Aparicio,<sup>\*,†</sup> Rafael Alcalde,<sup>†</sup> José Luis Trenzado,<sup>‡</sup> María N. Caro,<sup>§</sup> and Mert Atilhan<sup>⊥</sup><sup>†</sup>Department of Chemistry, University of Burgos, 09001, Burgos, Spain<sup>‡</sup>Department of Physics, University of Las Palmas de Gran Canaria, 35017 Las Palmas de Gran Canaria, Spain<sup>§</sup>Department of Chemistry, University of Las Palmas de Gran Canaria, 35017 Las Palmas de Gran Canaria, Spain<sup>⊥</sup>Department of Chemical Engineering, Qatar University, 2713 Doha, Qatar

## Supporting Information

**ABSTRACT:** The unusual properties of poly(ethyleneoxide) + alcohol mixtures were analyzed using a poly(ethylene oxide) monomer (1,2-dimethoxyethane) in ethanol solutions as a model. A collection of thermophysical measurements and computational studies, using density functional theory and classical molecular dynamics approaches, provide valuable information about the molecular-level structure of this mixture and on the interaction between 1,2-dimethoxyethane and ethanol molecules. Thermophysical measurements show remarkable deviations from ideality, which are related to the development of intermolecular hydrogen bonding between both molecules upon mixing and to the balance of homo- and heteroassociations. Density functional theory allows better characterization from energetic and structural viewpoints. In this work, the characteristics for the different 1,2-dimethoxyethane/ethanol hydrogen-bonding complexes are analyzed via atoms in a molecule and natural bond orbital methods. Classical molecular dynamics simulations are carried out for pure 1,2-dimethoxyethane and for mixtures in the whole composition range. Force field validation is done by comparison of predicted thermophysical properties with measured ones and through the analysis of 1,2-dimethoxyethane conformers. Structural features are inferred from the analysis of radial and distribution functions and their evolution with composition, together with the study of molecular distribution in the mixed fluids (microheterogeneities). Dynamic aspects of the mixtures' behavior are inferred from the calculated self-diffusion constants and mean square displacements. The whole study points to a highly structured fluid, whose structure is determined by the balance of the 1,2-dimethoxyethane disrupting effect on the ethanol hydrogen-bonding network and the appearance of microheterogeneities.



## INTRODUCTION

Poly(ethylene oxide) (PEO,  $\text{H}-(\text{O}-\text{CH}_2-\text{CH}_2)_n-\text{OH}$ ) is an important member of the polyethers family. PEO is an amphiphilic polymer that is soluble in water<sup>1,2</sup> and also in a wide range of common organic solvents, such as methanol, acetonitrile, dioxane, chloroform, and benzene.<sup>3</sup> PEO is a large molecular mass polymer, in which the effect of the terminal hydroxyl groups is negligible, and thus, the PEO properties in solution rise from the ether/ethyl groups. PEO is a low toxic<sup>4</sup> and readily biodegradable polymer<sup>5</sup> and is used in many relevant applications, such as drug delivery,<sup>6</sup> production of lithium polymer batteries,<sup>7</sup> fuel cells,<sup>8</sup> or polymer electrolyte membranes.<sup>9</sup> The behavior of PEO in water solution has attracted a wide attention, and thus, a large number of experimental and computational studies have been published in the last years.<sup>10–13</sup> The interest on the study of PEO + water systems rises from the fact that most of PEO applications rely on its high water solubility and on the use of a PEO + water system to mimic protein + water interactions (i.e., hydrogen bonding and hydrophobic interactions). By fitting the ethylene oxide units into the liquid water structure,<sup>2</sup> the properties of PEO in water solutions have been explained previously; however, this

has been criticized by some authors due to a balance or entropic/energetic factor.<sup>14</sup> In contrast, despite the fact of the wide interest of the behavior of PEO in water solutions, studies of this polymer in other relevant fluids are scarce. A study by Ho et al.<sup>15</sup> reported a very unusual phase behavior in PEO/ethanol mixtures: PEO does not dissolve in ethanol at room temperature, but when the temperature is increased above the crystal melting temperature of PEO, the polymer dissolves in ethanol. Yet, if it is quenched down to room temperature, it leads to a new lamellar-type structure. The PEO + ethanol system shows an upper critical solution temperature, which is below the PEO crystal melting point; therefore, crystallization appears before the phase separation. Moreover, water addition to PEO + ethanol solutions has remarkable effects on the phase behavior of the system, leading to the destruction of the crystalline morphology and yielding regular polymer solution behavior.<sup>16</sup> Therefore, the study of PEO + ethanol solutions has a remarkable interest considering these unusual properties.

Received: March 29, 2011

Revised: June 7, 2011

Published: June 09, 2011

1,2-dimethoxyethane (DME) is the shortest and simplest ether molecule having the local conformational properties of PEO, and it has been widely studied in the literature to model PEO interactions with solvents, especially its solutions in water.<sup>17–19</sup> Therefore, in this work, we report a study on DME + ethanol systems for which the intermolecular forces and structural features that govern the PEO + ethanol systems are investigated as a model in detail for the whole mole fraction range. This work is performed based on two complementary approaches. First, an experimental study is carried out, in which required relevant thermophysical properties are measured. Second, computational density functional theory (DFT) calculations together with atoms in a molecule (AIM) and natural bond orbitals (NBO) methods have been performed in order to analyze short-range interactions along with a molecular-level structural investigation by using classical molecular dynamics (MD) on the same experimented fluids.

## MATERIALS AND METHODS

**Materials.** DME (CAS no.110-71-4, purchased from Fluka, 99.5% purity from gas chromatography) and ethanol (CAS no. 64-17-5, purchased from Panreac, 99.8% gas chromatography purity) were used for all the experiments. Pure fluids were degassed with ultrasound, stored out of light over Fluka Union Carbide 0.4 nm molecular sieves, and used without further purification. Mixture samples were prepared by weighing with a Mettler AE240 balance ( $\pm 1 \times 10^{-5}$  g), thus leading to an accuracy of  $\pm 1 \times 10^{-4}$  for mole fraction.

**Thermophysical Properties.** All thermophysical measurements were performed at ambient pressure conditions. Density ( $\rho$ ) was measured with an Anton Paar DMA 60/602 densimeter instrument, which works based on monitoring the vibrating frequency of an oscillating U-tube in a fluid method. The densimeter cell temperature was controlled by a Polyscience 9010 circulating bath and measured by platinum resistance thermometers (PRT) by using ITS-90 reference standards with the accuracy of  $\pm 1.10^{-2}$  K. Densimeter calibrations were carried out using two reference standards: water (conductivity =  $5.5 \times 10^{-8} \Omega^{-1} \text{cm}^{-1}$  at 298.15 K) and *n*-heptane (Fluka, 99.5% purity), whose reference density values were obtained from the literature.<sup>20,21</sup> Therefore, considering all the error sources, density values were measured within an uncertainty of  $\pm 2 \times 10^{-5} \text{g cm}^{-3}$ .

Kinematic viscosity ( $\nu$ ) was measured using an automated Schott-Geräte AVS-350 capillary viscometer. The cell temperature was controlled through a Schott-Geräte CT1450/2 thermostat bath and measured with a PRT with an accuracy of  $\pm 1.10^{-2}$  K. The flow time was measured to  $\pm 1 \times 10^{-2}$  s. Calibration was performed by the manufacturer and certified to traceable procedures. The average uncertainty of the measured kinematic viscosity was 0.2%. Dynamic viscosity was calculated by using the experimental density and kinematic viscosity values within the accuracy of  $\pm 1 \times 10^{-2}$  mPa s.

**Density Functional Theory Calculations.** DFT calculations were carried out with the Gaussian 03 package<sup>22</sup> using the Becke gradient corrected exchange functional<sup>23</sup> and Lee–Yang–Parr correlation functional<sup>24</sup> with the three-parameters (B3LYP)<sup>25</sup> method. A 6-311++g\*\* basis set was used in this work. Atomic charges were calculated to fit the electrostatic potential<sup>26</sup> according to the Merz–Singh–Kollman (MK)<sup>27</sup> scheme. Interaction energies for DME + ethanol complexes,  $\Delta E$ , were calculated as

the differences among the complex and sum of corresponding monomer energies at the same theoretical level, with the basis set superposition error (BSSE) corrected through the counterpoise procedure.<sup>28</sup> Calculations in solution were carried out using the self-consistent reaction field approach (SCRF) with the solvent treated as a continuum using the integral equation formalism of the PCM approach (IEF-PCM).<sup>29</sup> The cavity in which the solute is placed in the IEF-PCM approach was built using the united atom model in all the cases; a value of 1.2 was used to scale all the radii and 70 tesserae to divide the spherical surfaces. AIM calculations<sup>30</sup> were carried out using the AIM2000 program.<sup>31</sup> NBO<sup>32</sup> studies were also performed. AIM and NBO calculations were done for the optimized structures in gas phase.

**Molecular Dynamics Simulations.** Classical molecular dynamics simulations were carried out using the TINKER molecular modeling package.<sup>33</sup> All simulations were performed in an NPT ensemble; the Nosé–Hoover method<sup>34</sup> was used to control the temperature and pressure of the simulation system. The motion equations were solved using the Verlet Leapfrog integration algorithm.<sup>35</sup> Long-range electrostatic interactions were treated with the smooth particle mesh Ewald method.<sup>36</sup> The simulated systems consist of cubic boxes with a total of 500 molecules with both pure DME and ethanol mixtures. Periodic boundary conditions were applied in three directions for the simulation box. The simulations were performed using a cutoff radius of  $L/2 \text{ \AA}$  for the nonbonded interactions,  $L$  being the initial box side. Initial boxes were generated using the PACKMOL program<sup>37</sup> to obtain adequate starting configurations. The energy of these boxes was minimized by using the MINIMIZE program in the TINKER package to a  $0.01 \text{ kcal mol}^{-1} \text{ \AA}^{-1}$  rms gradient; then several heating and quenching steps in the NVT ensemble up to 500 K were performed, after which a 100 ps NVT equilibration molecular dynamics simulation was carried out at the set temperature. Finally, from the output NVT simulation configuration, a run of 500 ps (time step of 1 fs) in the NPT ensemble at the set temperature and pressure was carried out, the first 100 ps being used to ensure equilibration, which is checked through constant energy, and the remaining 400 ps for data collection. Ethanol and DME were described according to the optimized potential for liquid simulations (all-atom version) OPLS-AA.<sup>38</sup> Force field parameters for ethanol were obtained from the original OPLS-AA parametrization,<sup>38</sup> except charges that were obtained from MK values obtained, as explained in the previous section. Several force field DME parametrizations are available in the literature;<sup>18,19</sup> the main differences between them rise from the values of parameters for the torsional O–C–C–O and C–O–C–C contributions, which have a strong effect on the distribution of the different DME conformers. The DME parameters used in this work come from the original OPLS-AA parametrization<sup>38</sup> with the exception of O–C–C–O and C–O–C–C, for which the ab initio torsional profiles obtained by Anderson and Wilson<sup>18</sup> were fitted to the OPLS-AA torsional equation (with three terms). The DME Coulombic term was treated using MK charges as for ethanol. All the force field parameters are available in the Supporting Information (Tables S1 and S2).

## RESULTS AND DISCUSSION

**Properties of Pure DME in the Liquid Phase.** The thermophysical properties, density, and viscosity for pure DME are reported as a function of temperature in Table S3 (Supporting

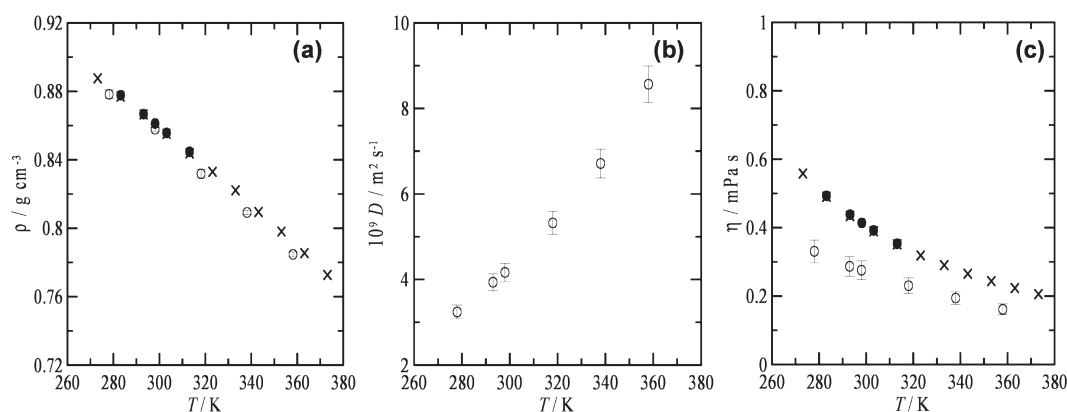


**Figure 1.** Comparison between experimental and predicted thermophysical properties for pure DME as a function of temperature and isobaric conditions ( $\sim 0.1$  MPa).  $\rho$  stands for density,  $D$  for the self-diffusion coefficient, and  $\eta$  for dynamic viscosity. Symbols: (●) experimental data obtained in this work (values from Table S3, Supporting Information), (×) experimental data from Zheng et al.,<sup>44</sup> and (○) predicted values from NPT molecular dynamics simulations (force field parameters from Table S1, Supporting Information). Error bars are plotted only for calculated data; for experimental data, error bars are lower than plotted symbols.

Information). These properties were used to validate force field parametrization through the comparison between experimental and predicted data from molecular dynamics simulations. Density predictions as a function of temperature at isobaric conditions may be obtained simply via molecular dynamics simulations in the NPT ensemble; however, to infer dynamic viscosity values from simulations is not straightforward. Shear viscosity values may be obtained from equilibrium molecular dynamics through two main approaches: (i) Green–Kubo and (ii) Stokes–Einstein methods.<sup>39,40</sup> The Green–Kubo approach requires too long simulations to ensure the reliability of the inferred values because of the slow convergence of the involved integrals because of the small fluctuations of the off-diagonal elements of the pressure tensor. Therefore, we have used in this work the Stokes–Einstein method in which self-diffusion coefficients are calculated using Einstein’s method, eq 1, and then viscosity values are calculated from eq 2:

$$D = \frac{1}{6} \lim_{t \rightarrow \infty} \frac{\langle \Delta r(t)^2 \rangle}{t} \quad (1)$$

$$\eta = \frac{k_B T}{6\pi D r} \quad (2)$$

In eq 1, the quantity in brackets stands for the mean square displacement (msd), and in eq 2,  $k_B$  stands for the Boltzmann’s constant,  $T$  stands for the temperature, and  $r$  is the effective hydrodynamic radius. Stokes–Einstein, eq 2, was applied using stick boundary conditions, although it is not strictly applicable due to the close relative sizes of the involved species (pure fluid).<sup>41</sup> Viscosity prediction from Stokes–Einstein’s method requires the knowledge of the hydrodynamic radius for DME, and this value was obtained from the literature. Kuga<sup>42</sup> and Lee et al.<sup>43</sup> reported  $r$  values for PEO as a function of the number of  $n$ -mers in the polymer chain. These reported values were plotted in a log–log plot as a function of the number of  $n$ -mers, fitted to a linear equation and extrapolated to  $n = 1$  (DME), which resulted with the calculated value for DME as  $r = 1.9$  Å, which was used in this work for viscosity predictions from molecular dynamics simulations. A comparison between experimental and predicted density and viscosity data together with calculated self-diffusion constants for pure DME is reported in Figure 1. Predicted density

values are in good agreement with the experimental data in the studied temperature range (Figure 1a). The absolute average percentage deviation (% AAD) between NPT molecular dynamics predictions and experimental density data reported in this work is 0.63%, whereas the deviation with data reported by Zheng et al.<sup>44</sup> is 0.68%. In the open literature, there is no experimental self-diffusion ( $D$ ) data available reported as a function of temperature for pure DME. Bedrow et al.<sup>45</sup> reported proton NMR pulse-field gradient measurements for pure DME at 298 K and obtained a  $D$  value of  $0.32 \times 10^{-8} \text{ m}^2 \text{s}^{-1}$ , which is in good agreement with the predicted value obtained in this work ( $0.42 \times 10^{-8} \text{ m}^2 \text{s}^{-1}$ ). Therefore, it may be concluded that the translational dynamics of pure DME is correctly reproduced by the proposed force field parametrization. The predicted change of  $D$  with temperature is reported in Figure 1b, which, fitted to an Arrhenius type behavior ( $r = 0.9964$ ), leads to an activation barrier for diffusion of  $10.0 \text{ kJ mol}^{-1}$ . Predicted viscosity data are lower than experimental values; see Figure 1c. Nevertheless, the calculated activation energy for viscous flow, obtained using the Arrhenius equation ( $r = 0.9950$ ), is  $7.4 \text{ kJ mol}^{-1}$ , which compares acceptably well with  $8.2$  and  $8.4 \text{ kJ mol}^{-1}$  values obtained from experimental viscosity data reported in this work and those reported by Zheng et al.,<sup>44</sup> respectively. Another useful property for the analysis of the performance for the proposed force field parametrization is vaporization enthalpy,  $\Delta H_{\text{vap}}$ , and it is calculated from molecular dynamics simulations according to eq 3

$$\begin{aligned} \Delta H_{\text{vap}} &= \Delta U_{\text{L,G}} + RT \\ &= (U_{\text{G,inter}} - U_{\text{L,inter}}) + (U_{\text{G,intra}} - U_{\text{L,intra}}) + RT \end{aligned} \quad (3)$$

where  $U$  stands for the molar internal energy of the liquid, L, and gas, G, phases. “Intra” and “inter” refer to intramolecular (bond, angle, and dihedral contributions together with nonbonded intramolecular interactions) and intermolecular (Coulombic and van der Waals interactions) contributions to the internal energy. To calculate properties for the gas phase, a single DME molecule was simulated. Therefore, we obtain  $\Delta H_{\text{vap}}(298 \text{ K}) = 36.1 \pm 0.3 \text{ kJ mol}^{-1}$ , which is in very good agreement with the experimental value of  $\Delta H_{\text{vap}}(298 \text{ K}) = 36.4 \text{ kJ mol}^{-1}$  reported in the literature.<sup>46</sup> Hence, the force field parametrization may be considered as satisfactory, within reasonable limits because of the purely predictive character of the simulations and the complexity



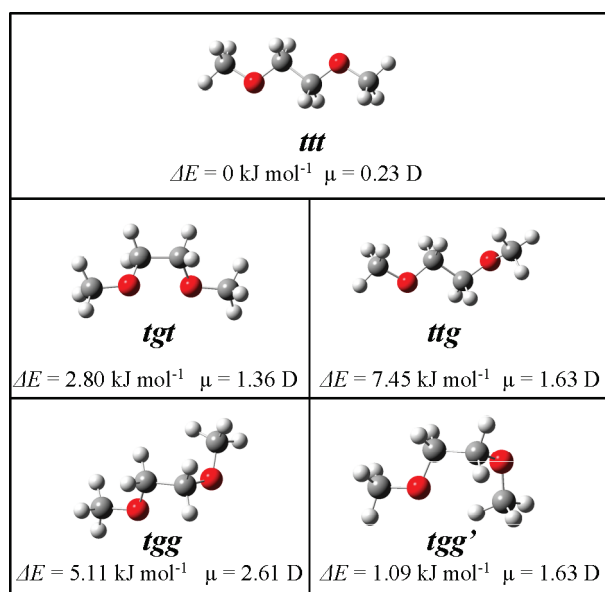


**Figure 2.** Low-energy conformers of DME calculated at the B3LYP/6-311++g\*\* theoretical level in gas phase.  $\Delta E$  stands for the energy difference with the lowest-energy conformer (ttt) and  $\mu$  for the calculated dipole moment.

of the involved molecule, and thus, reliable structural information may be inferred from this study. The larger deviations between the studied properties rise from viscosity predictions; this problem may rise not from the used parametrization but from the equations used to infer this property and the poor characterization of the applied hydrodynamic model. Nevertheless, it should be remarked the complexity of predicting viscosity from molecular dynamics simulations even for small molecules.<sup>47</sup>

Liquid DME is characterized by the presence of several conformers, whose relative populations have been analyzed previously in the literature.<sup>18,19</sup> Five main DME conformers may be found in the liquid state, and those are named according to the gauche or trans positions of the C–O–C–C and central O–C–C–O dihedrals: ttt, tgt, ttg, tgg, and tgg'. To get a deeper insight into the properties of these conformers, we carried out quantum chemistry B3LYP/6-311++g\*\* calculations in the gas phase (Figure 2). Calculated results show that the energy ordering is  $\text{ttt} < \text{tgg}' < \text{tgt} < \text{tgg} < \text{ttg}$ . Although the energy differences between the different conformers are not too large, these results are in agreement with previous literature computational<sup>18</sup> and IR gas-phase studies.<sup>48</sup> The factors leading to the conformational stability of the five main conformers of DME were analyzed by Goutev et al.<sup>49</sup> based on energetic and entropic factors together with the suggestion of the possible effect of multipoles on their relative stabilities. Goutev et al.<sup>49</sup> reported a change in the relative population of conformers on going from the gas to the liquid phase for pure DME; their results obtained from Raman spectroscopy measurements together with quantum chemistry calculations led to a population of  $\text{tgt} > \text{tgg}' > \text{ttt} > \text{tgg} > \text{ttg}$ , at low temperatures, with a remarkable increase of the tgg' population with increasing temperature in such a way that the tgg' conformer would be the prevailing one at high temperatures. The stabilization of the tgt isomer on going to the liquid phase at the expense of the ttt conformer, which is the most populated conformer in the gas phase, rises from the appreciable dipole moment of the tgt conformer in comparison with the almost null

value for ttt. There is some controversy on the factors leading to the stabilization of the tgg' conformer in the liquid phase. Some authors have showed the prevailing role for the stabilization of the tgg' conformer rising from the weak  $\text{CH} \cdots \text{O}$  intramolecular hydrogen bonding.<sup>18,50</sup> Smith et al.<sup>51</sup> proposed that the intramolecular hydrogen bond is replaced by the stronger intermolecular  $\text{CH} \cdots \text{O}$  interaction, which would have a remarkable effect on the tgg' population, although this argument is in contrast with the large tgg' population in the liquid phase, as Goutev et al.<sup>49</sup> showed. Moreover, we have analyzed the characteristics of the  $\text{CH} \cdots \text{O}$  intramolecular interaction using the AIM approach in this work. According to the AIM theory, two criteria must be satisfied to confirm the existence of H-bonding:<sup>52,53</sup> (i) a bond path between two atoms with the existence of a bond critical point, BCP, in the middle of the path and (ii) electron density at BCP,  $\rho_{\text{BCP}}$ , and the Laplacian of that electron density,  $\nabla^2 \rho_{\text{BCP}}$ , must be within the 0.002–0.035 and 0.024–0.139 ranges, respectively, (both in atomic units). The AIM analysis leads to  $\rho_{\text{BCP}} = 0.010 \text{ au}$  and  $\nabla^2 \rho_{\text{BCP}} = 0.009 \text{ au}$  for tgg'  $\text{CH} \cdots \text{O}$  intramolecular hydrogen bonding. These values are close to the lower limit (even  $\nabla^2 \rho_{\text{BCP}}$  is below the lower limit), and thus, hydrogen bonding has to be ruled out or considered a very weak interaction in the gas phase. Therefore, to justify the increasing tgg' population in the liquid phase, it could be argued that some stabilization of the  $\text{CH} \cdots \text{O}$  intramolecular interaction rises on going to the liquid phase, because the competing effect of intermolecular  $\text{CH} \cdots \text{O}$  interaction should be discarded.<sup>49</sup> Likewise, we have analyzed the characteristics of the tgg' conformer in solution using the IEF-PCM approach in which the solvent media are treated as a continuum with a dielectric constant  $\epsilon = 7.3$  (neat liquid DME) and compared with the gas phase results, both at the same theoretical level. The vibrational spectra of the tgg' conformer in gas phase and IEF-PCM are plotted in Figure S1 (Supporting Information). The assignment of the bands is out of the scope of this work, and it was previously done by Yoshida et al.<sup>54</sup> Nevertheless, the spectra reported in Figure S1 (Supporting Information) show a clear red shifting on going from the gas phase to solution (as simulated using the IEF-PCM approach), and thus, the possible weak intramolecular hydrogen bonding seems to be slightly strengthened on going to the liquid phase, which would justify the large tgg' populations. Likewise, NBO analysis for the tgg' conformer in gas phase does not show any hyperconjugation-induced charge transfer between DME oxygen and opposite terminal hydrogens in the tgg' conformer, which again discards intramolecular hydrogen bonding.

Conformer populations for liquid DME were also analyzed from molecular dynamics simulations, and the percentage values obtained were 48, 16, 6, 3, and 27% for tgt, ttt, tgg, ttg, and tgg', respectively, which is in good agreement with experimental values.<sup>49</sup> Radial distribution functions, RDFs, for pure liquid DME are reported as a function of temperature in Figure 3 together with number integrals,  $N$ , calculated according to eq 4

$$N = \rho \int_0^r g(r) 4\pi r^2 dr \quad (4)$$

where  $\rho$  stands for the bulk number density and  $g(r)$  for the corresponding radial distribution function. RDFs are highly structured with a first peak at 4.75 Å, followed by a shoulder

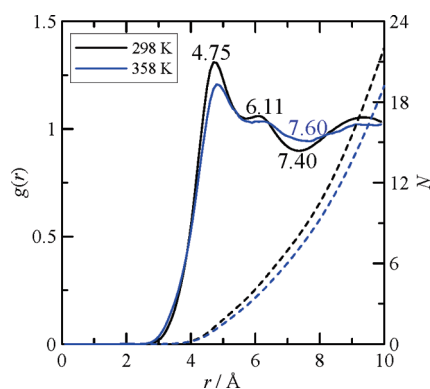


**Figure 3.** Center of mass radial distribution functions,  $g(r)$ , for pure DME as a function of temperature at  $\sim 0.1$  MPa, from NPT molecular dynamics simulations (force field parameters from Table S1, Supporting Information).  $r$  values for  $g(r)$  maxima and minima are reported inside the panel.

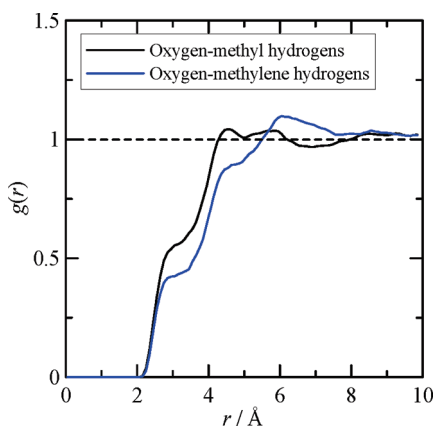


**Figure 4.** Site-site radial distribution functions,  $g(r)$ , for pure DME as a function of temperature at  $\sim 0.1$  MPa, from NPT molecular dynamics simulations (force field parameters from Table S1, Supporting Information).

at 6.11 Å extending up to minima around 7.40–7.60 Å. The intensity of these peaks decreases with increasing temperature, but structuring is maintained up to high temperatures. For example, RDFs reported at 358 K in Figure 3 are functions obtained at the normal boiling temperature ( $358 \pm 1$  K).<sup>55</sup> Nevertheless, RDFs reported in Figure 4 for the interaction between DME oxygens and terminal hydrogens (methyl hydrogens) or inner hydrogens (methylene hydrogens) do not show hydrogen bonding between these molecules. Moreover, intermolecular interaction energies and electrostatic and Lennard-Jones contributions, reported in Figure 5, show remarkably large values, especially for the Lennard-Jones contribution, which are only slightly weakened with increasing temperature.

**Analysis of the DME + Ethanol Interaction Using Quantum Chemistry Methods.** The properties of the DME + ethanol interactions, hydrogen bonding, are studied for the five most populated isomers using quantum chemistry methods together with AIM and NBO approaches, in the gas phase. These results would lead to valuable information about the short-range interactions in liquid DME–ethanol mixtures, and they would allow analyzing how the conformation of DME molecules affects the interaction with ethanol molecules.

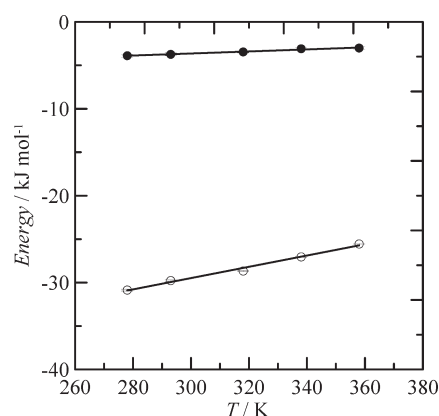


**Figure 5.** Intermolecular energy contributions for pure liquid DME as a function of temperature at  $\sim 0.1$  MPa from NPT molecular dynamics simulations (force field parameters from Table S1, Supporting Information). Symbols: filled circles, electrostatic contribution; empty circles, Lennard-Jones contribution.

Counterpoise corrected interaction energies for DME–ethanol 1:1 complexes are reported in Table 1 together with the most remarkable information extracted from AIM/NBO analyses. The optimized structures for the DME–ethanol pairs are reported in Figure S2 (Supporting Information), and the calculated ordering of interaction energies is  $\text{tgt} > \text{tgg}' > \text{ttg} > \text{ttt} > \text{tgg}$ . Bond paths and BCPs for the five studied complexes are reported in Figure S3 (Supporting Information).  $\rho_{\text{BCP}}$  and  $\nabla^2\rho_{\text{BCP}}$  values reported in Table 1 are in the upper limit of the AIM hydrogen-bonding range and thus point to moderately strong hydrogen bonding, which is in agreement with the interaction energies reported in Table 1. Moreover, the larger the  $\rho_{\text{BCP}}$  and  $\nabla^2\rho_{\text{BCP}}$ , the stronger the hydrogen bonding, and thus the larger the interaction energies; this rule is fulfilled for all the studied conformers with the exception of  $\text{tgt}$ .

NBO main results are reported in Table 1. Hydrogen bonding may be studied according to the NBO approach analyzing the charge transfer between the involved donor and acceptor centers. In the studied complexes reported in Figure S2 (Supporting Information), hydrogen bonding rises from the hyperconjugation-induced charge transfer between lone pairs in DME oxygen (donor) and the antibonding orbitals in the ethanol OH group (acceptor), that is to say:  $n_{\text{O(DME)}} \rightarrow \sigma^*_{\text{OH(ethanol)}}$ . Three main properties are used to analyze NBO results: second-order perturbation energy,  $E(2)$ , energy difference among donor and acceptor,  $\Delta E_{\text{D-A}}$ , and Fock matrix element between donor and acceptor,  $F_{\text{D-A}}$ , this last property reflecting the symmetry between donor and acceptor. It may be shown that the larger the  $E(2)$ , the stronger the hydrogen bonding, which is fulfilled by all the studied complexes, with the exception of  $\text{tgt}$  ones.  $E(2)$  may be larger because of a low  $\Delta E_{\text{D-A}}$  or a large  $F_{\text{D-A}}$ , which facilitates charge transfer because of low-energy differences or good symmetry between donor and acceptor, respectively. Results reported in Table 1 show  $\Delta E_{\text{D-A}}$  values equal for all the involved donors and acceptors, and thus, the strength of the hydrogen bonding rises from symmetry factors, measured by  $F_{\text{D-A}}$ . Charge transfer from the first oxygen lone pair in DME is more difficult than transfer from the second pair because of the larger  $\Delta E_{\text{D-A}}$  values, but symmetry operates in the opposite direction, this fact being more important as the larger  $E(2)$  values for the transfer from the first pair show. Therefore, the strength of

**Table 1. Quantum Chemistry Results for the Study of DME–Ethanol 1:1 Complexes for the Five Most Relevant DME Conformers<sup>a,b</sup>**

DME conformer	$\Delta E/\text{kJ mol}^{-1}$	$\rho_{\text{BCP}}/\text{au}$	$\nabla^2\rho_{\text{BCP}}/\text{au}$	$\Delta E_{\text{D}-\text{A}}/\text{au}$	$E(2)/\text{kJ mol}^{-1}$	$F_{\text{D}-\text{A}}/\text{au}$
ttt	−18.33	0.026	0.092	1.04/0.78	15.56/12.64	0.056/0.044
tgt	−20.84	0.021	0.080	1.04/0.78	7.41/10.54	0.038/0.040
ttg	−19.16	0.026	0.092	1.03/0.78	12.97/15.98	0.051/0.050
tgg	−16.82	0.023	0.084	1.03/0.78	10.67/10.79	0.046/0.041
tgg′	−20.46	0.027	0.100	1.03/0.78	19.12/10.59	0.062/0.040

<sup>a</sup>  $\Delta E$ , counterpoise corrected interaction energy;  $\rho_{\text{BCP}}$ , electron density at the bond critical point (BCP);  $\nabla^2\rho_{\text{BCP}}$ , Laplacian of electron density at BCP;  $E(2)$ , second-order perturbation energy;  $\Delta E_{\text{D}-\text{A}}$ , energy difference among donor and acceptor;  $F_{\text{D}-\text{A}}$ , Fock matrix element between donor and acceptor. <sup>b</sup> All values calculated at the B3LYP/6-311++g\*\* theoretical level in gas phase. AIM and NBO properties reported for the hydrogen bonds are plotted in Figure S2 (Supporting Information). For  $E(2)$ ,  $\Delta E_{\text{D}-\text{A}}$ , and  $F_{\text{D}-\text{A}}$ , the two values reported in each column correspond to the donation of each DME oxygen lone pairs (for the DME oxygen involved in the hydrogen bonding) to the corresponding orbital in the ethanol OH group (Figure S2, Supporting Information). For  $\rho_{\text{BCP}}$ , and  $\nabla^2\rho_{\text{BCP}}$ , values correspond to the BCPs reported in Figure S3 (Supporting Information).

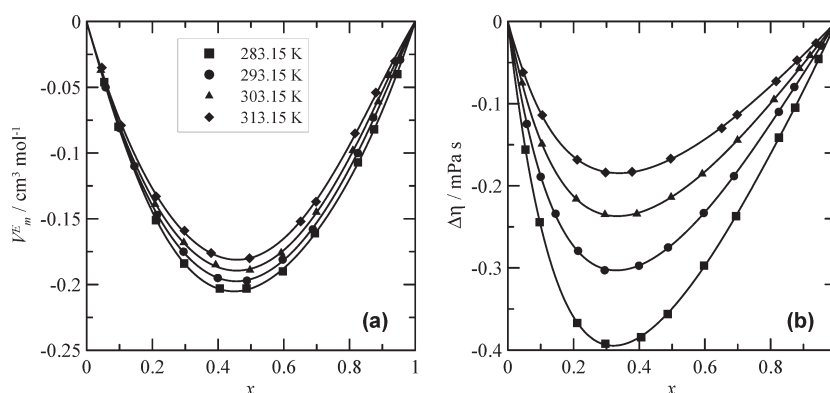


**Figure 6.** Experimental excess molar volume,  $V_m^E$ , and mixing viscosity,  $\Delta\eta$ , for  $x\text{DME} + (1 - x)\text{ethanol}$  as a function of temperature at  $\sim 0.1$  MPa. Symbols: filled symbols, data obtained from experimental density; lines, fitting for guiding purposes.

DME–ethanol interactions, for the five studied conformers, is clearly controlled by symmetry factors: the most adequate donor–acceptor symmetry, the stronger the hydrogen bonding. The exception is the tgt–ethanol interaction, for which the remarkably low energy difference between the donor and the acceptor leads to the strongest hydrogen bonding between the studied ones, despite the poor donor–acceptor symmetry.

**Analysis of the DME + Ethanol Interaction in the Liquid Phase.** Experimental density and dynamic viscosity data, and their derived excess volume ( $V_m^E$ ) and mixing viscosity ( $\Delta\eta$ ) properties (defined to well-known relationships),<sup>56,57</sup> analyzed together with the results obtained from molecular dynamics simulations, allow inferring the main structural features in the DME + ethanol liquid mixture as a function of temperature.

Excess volume and mixing viscosity are reported in Figure 6; both properties are negative in the whole composition range and decrease (in absolute value) with increasing temperature. The negative sign of both properties points to two main structural features: (i) the effective packaging of both molecules and (ii) the formation of DME + ethanol hydrogen bonding upon mixing do not compensate the breaking of the ethanol–ethanol hydrogen-bonding structure in pure liquid ethanol.  $V_m^E$  minima appear for  $x = 0.45$ , and thus, the most effective packing is produced for almost equimolar mixtures, which may be justified considering the sizes and shapes of both molecules. The Connolly solvent-excluded volume is in the 88.3–89.1 Å<sup>3</sup> for the five most populated DME isomers (calculated from the optimized gas-phase structures reported in previous sections) and 45.4 Å<sup>3</sup> for

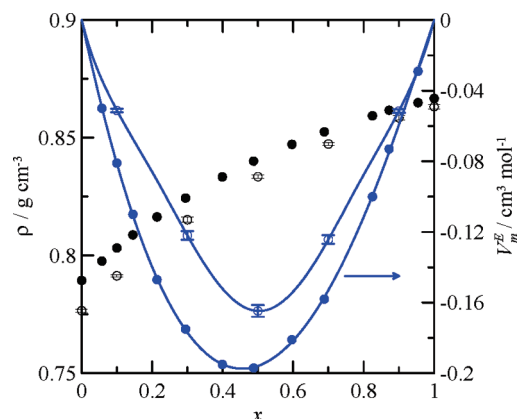


**Figure 7.** Comparison between experimental (Table S4, Supporting Information) and predicted density,  $\rho$ , and excess molar volume,  $V_m^E$ , for  $x\text{DME} + (1 - x)\text{ethanol}$  at 293 K/ $\sim 0.1$  MPa. Symbols: filled circles) experimental data; empty circles, predicted values from NPT molecular dynamics simulations (force field parameters from Table S1, Supporting Information); black symbols,  $\rho$ ; blue symbols,  $V_m^E$ . Lines are plotted for guiding purposes. Error bars are plotted only for calculated data; for experimental data, error bars are lower than plotted symbols.

ethanol; therefore, the size of DME isomers is almost double that of ethanol molecules. The calculated free volumes (obtained using the calculated values of Connolly solvent-excluded volumes and the experimental molar volume) are 33.96 and 55.60 cm<sup>3</sup> mol<sup>−1</sup>, for

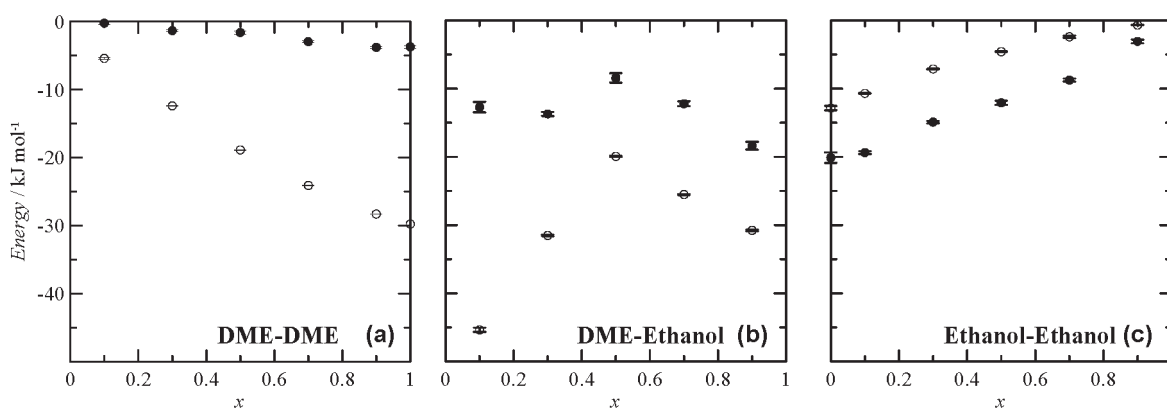


**Figure 8.** Intermolecular energy contributions for  $x$ DME +  $(1 - x)$ ethanol at 293 K/ $\sim$ 0.1 MPa from NPT molecular dynamics simulations (force field parameters from Table S1, Supporting Information). Symbols: filled circles, electrostatic contribution; empty circles, Lennard-Jones contribution. Each panel shows contributions for DME–DME, DME–ethanol, and ethanol–ethanol interactions.

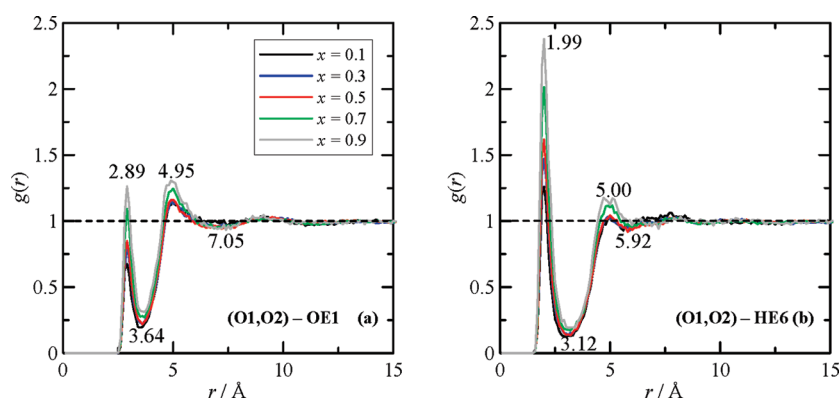


**Figure 9.** Site–site radial distribution functions,  $g(r)$ , around DME oxygen atoms for  $x$ DME +  $(1 - x)$ ethanol at 293 K/ $\sim$ 0.1 MPa, from NPT molecular dynamics simulations (force field parameters from Table S1, Supporting Information). Atom numbering as in Tables S1 and S2 (Supporting Information). Panels show  $g(r)$  for interactions between DME ether oxygens and ethanol hydroxylic oxygen (panel a) and ethanol hydroxylic hydrogen (panel b). Numeric values within each panel show  $r$  (Å) for maxima and minima.

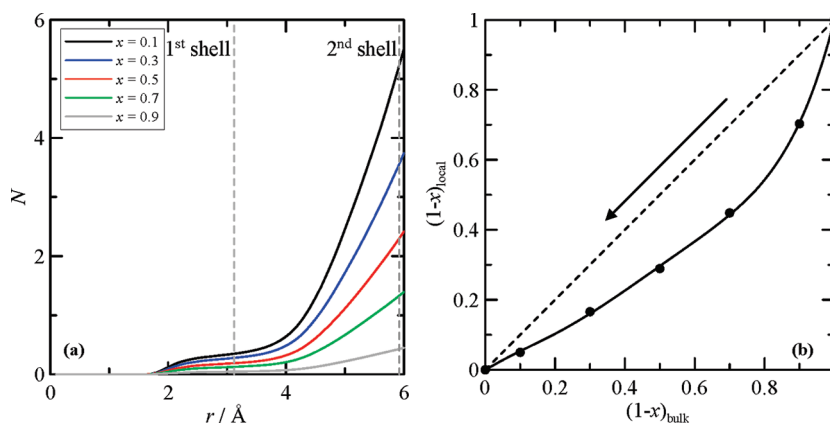


**Figure 10.** (a) Number integrals (eq 4) of ethanol hydroxylic hydrogens around DME ether oxygens (obtained from  $g(r)$  reported in Figure 9b) and (b) comparison between ethanol local (around DME ether oxygens, with  $r = 5.9$  Å, second minimum in Figure 8b) and bulk mole fractions, for  $x$ DME +  $(1 - x)$ ethanol at 293 K/ $\sim$ 0.1 MPa, from NPT molecular dynamics simulations (force field parameters from Tables S1 and S2, Supporting Information). In panel a, we show  $r$  values (dashed lines) for the first and second solvation shells obtained from Figure 9b (first and second minima). In panel b, the continuous line is shown for guiding purposes and the dashed line to indicate when the ethanol local mole fraction is equal to the bulk mole fraction. The arrow in panel b shows the increasing DME mole fraction for guiding purposes.

pure ethanol and DME, respectively, which represent 58.2 and 55.6% of the molar volume. Therefore, the packaging of DME

molecules in cavities of ethanol-rich mixtures is possible. Moreover, the shapes of DME and ethanol molecules are very similar;



the calculated ovality parameter, which measures the departure from a spherical shape, is in the 1.24–1.28 range for DME isomers and is 1.14 for ethanol, which favor the packing of both molecules in the available cavities for the studied mixed fluids. The mixing viscosity is negative in the whole composition range, with minima for  $x = 0.33$ . This behavior shows the prevailing effect of disrupting ethanol–ethanol hydrogen bonding, leading to less viscous fluids, this effect being more remarkable for ethanol-rich mixtures as the obtained minima show.

Although experimental reported thermophysical properties provide certain information about the behavior of the studied mixtures, the molecular level structure can be analyzed more in detail with the obtained molecular dynamics results that may shed light into the effects controlling the behavior of these fluids. The predictive ability of the proposed force field parametrization to describe the properties of the studied mixed fluid is reported in Figure 7; both the experimental density and the excess molar volume are predicted with good accuracy in the whole composition

range. The analysis of the DME–ethanol interaction is done from the viewpoint of intermolecular interaction energy in Figure 8, in which the intermolecular energy is split in homo (DME–DME and ethanol–ethanol) and hetero (DME–ethanol) contributions, both for electrostatic and Lennard-Jones terms. Values for pure ethanol (Figure 8c,  $x = 0$ ) show an electrostatic contribution larger than the Lennard-Jones one, which is in agreement with available previous simulations done by Pereira et al.,<sup>58</sup> who showed that the electrostatic term is 57.6% of the total intermolecular energy, which is 61.0% in this work. Intermolecular energies for pure DME (Figure 8a,  $x = 1$ ) are dominated by the Lennard-Jones term (88.9%). Moreover, total intermolecular interaction energies (electrostatic plus Lennard-Jones) are  $-33.5$  and  $-33.0$  kJ mol<sup>-1</sup> for pure DME and ethanol, respectively; these similar values are in agreement with the close values of vaporization enthalpies for both fluids ( $36.4$  and  $42.2$  kJ mol<sup>-1</sup> at 298.15 K, for DME and ethanol, respectively).<sup>46</sup> Nevertheless, DME intermolecular interactions are dominated by the

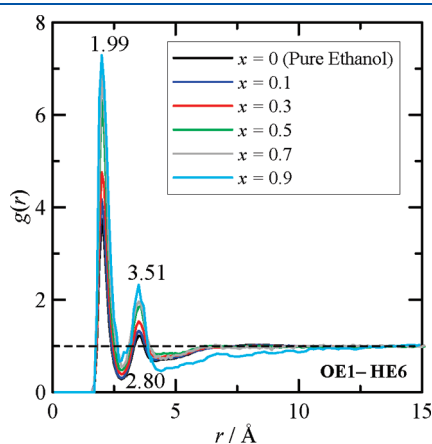


**Figure 11.** Site–site radial distribution functions,  $g(r)$ , of ethanol hydroxylic oxygen around ethanol hydroxylic hydrogen for  $x$ DME +  $(1 - x)$ ethanol at 293 K/ $\sim 0.1$  MPa, from NPT molecular dynamics simulations (force field parameters from Table S1, Supporting Information). Atom numbering as in Table S2 (Supporting Information). Numeric values show  $r$  (Å) for maxima and minima.

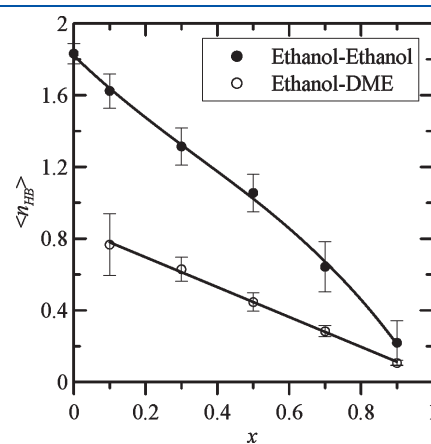


**Figure 13.** Mean number of hydrogen bonds,  $\langle n_{\text{HB}} \rangle$ , between ethanol molecules (ethanol–ethanol, per ethanol molecule) and between ethanol and DME molecules (ethanol–DME, per DME molecule) for  $x$ DME +  $(1 - x)$ ethanol at 293 K/ $\sim 0.1$  MPa, from NPT molecular dynamics simulations (force field parameters from Tables S1 and S2, Supporting Information).

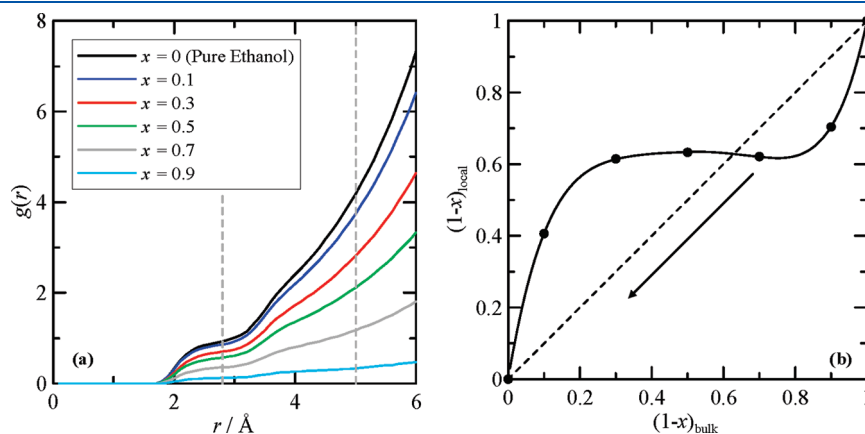


**Figure 12.** (a) Number integrals (eq 4) of ethanol hydroxylic hydrogens around ethanol hydroxylic oxygens (obtained from  $g(r)$  reported in Figure 11) and (b) comparison between ethanol local (around ethanol hydroxylic hydrogens, with  $r = 5.0$  Å, second minimum in Figure 11) and bulk mole fractions, for  $x$ DME +  $(1 - x)$ ethanol at 293 K/ $\sim 0.1$  MPa, from NPT molecular dynamics simulations (force field parameters from Tables S1 and S2, Supporting Information). In panel a, we show  $r$  values (dashed lines) for the first and second solvation shells obtained from Figure 11 (first and second minima). In panel b, the continuous line is shown for guiding purposes and the dashed line to indicate when the ethanol local mole fraction is equal to the bulk mole fraction. The arrow in panel b shows the increasing DME mole fraction for guiding purposes.



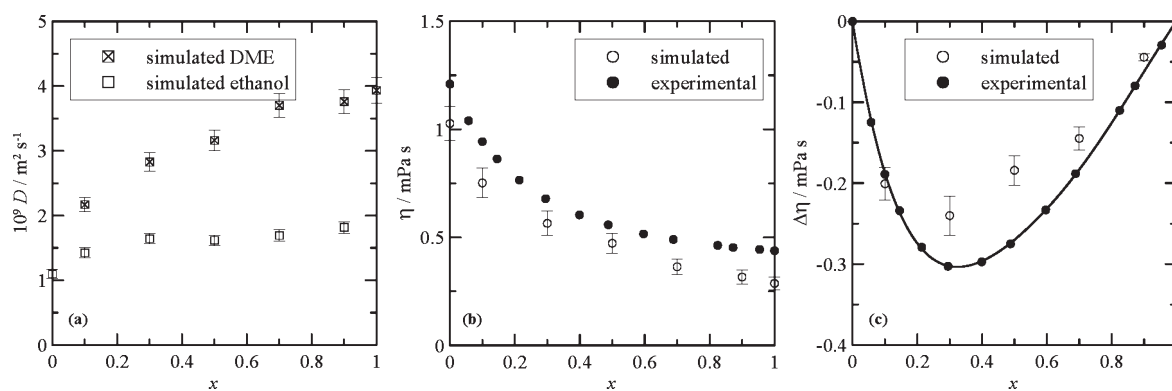


**Figure 14.** (a) Self-diffusion coefficients of DME and ethanol, (b) dynamic viscosity, and (c) mixing viscosity for  $x$ DME +  $(1 - x)$ ethanol at 293 K/ $\sim 0.1$  MPa. Simulated values obtained from NPT molecular dynamics simulations (force field parameters from Tables S1 and S2, Supporting Information). Experimental values obtained in this work.

Lennard-Jones type, whereas electrostatic prevails for pure ethanol. The ethanol–ethanol intermolecular energy decreases in an almost linear fashion with increasing DME mole fraction, whereas DME–DME increases. DME–ethanol heteroassociations show a complex behavior; the energy of these interactions is clearly dominated by the Lennard-Jones type, especially for low DME concentrations, for which a remarkably strong (effective) DME–ethanol interaction is obtained. Therefore, the ethanol–DME interaction is more favorable for low DME concentrations, whereas, for larger DME mole fractions, this interaction is weakened.

Structural effects may be analyzed using relevant RDFs; we report in Figure 9 RDFs for site–site interactions between ether oxygens in DME (hydrogen-bonding acceptors) and ethanol oxygen and hydroxylic hydrogen (hydrogen-bonding donor), as a function of mole fraction. Both RDFs reported in Figure 9 point to the development of ethanol–DME hydrogen bonding; ether oxygen–ethanol hydrogen RDFs show a sharp narrow first peak at 1.99 Å, whose position does not change with increasing DME mole fraction, with a first minima followed by a second wide peak at 5.00 Å. Number integrals reported in Figure 10a for ethanol hydroxylic hydrogen around ether oxygen show a first solvation shell with  $N = 0.34$  and a second one with  $N = 5.2$  for  $x = 0.1$ , and decreasing with increasing DME mole fraction. Therefore, the DME–ethanol interaction seems to be effective from the energetic viewpoint, as results reported in Figure 9b show, but the first solvation shell (very narrow) only allows the development of a reduced number of hydrogen bonds because of the competing effect of ethanol–ethanol interactions between the surrounding molecules. We report also in Figure 10b the ethanol local mole fraction<sup>59</sup> around DME oxygens (composition of the solvation shell), which is always lower than the bulk mole fraction for ethanol, thus pointing to a disrupting effect of DME molecules on the ethanol hydrogen-bonding network (ethanol molecules do not cluster around DME hydrogen-bonding acceptor sites), especially for low DME concentrations, which would justify the decreasing viscosity values and ethanol–ethanol interaction energy upon mixing. The effect of DME on ethanol structuring may be inferred from results reported in Figures 11 and 12. RDFs for ethanol–ethanol hydroxylic hydrogen–oxygen interactions show the characteristic first sharp, narrow, and very intense peak at 1.99 Å, followed by a second one, less intense, at 3.51 Å; the first shell integrates to  $N = 0.87$  and the second shell to  $N = 2.82$ , for a DME mole fraction equal to 0.1, and decreasing with

increasing DME concentration (Figure 12a). The ethanol local mole fraction around ethanol molecules (Figure 12b) is lower than the bulk ethanol mole fraction for low DME concentrations (disrupting effect of DME molecules) and larger for large DME mole fractions. Therefore, ethanol molecules tend to cluster toward DME-rich mixtures.

The calculated average number of hydrogen bonds ( $\langle n_{\text{HB}} \rangle$ ), ethanol–ethanol and DME–ethanol, are reported in Figure 13. RDF results reported in Figures 9 and 11 report two well-defined types of interactions through hydrogen bonding: DME–ethanol and ethanol–ethanol in the whole composition range. We define each hydrogen-bonding occurrence for distances up to the first minima in the corresponding RDF (1st solvation shells). No remarkable effect of considered angles, within reasonable values, was found on the extension of hydrogen bonding, and thus, a  $50^\circ$  value was used for all the possible interactions. Results for pure ethanol (Figure 13,  $x = 0$ ) at 293 K/0.1 MPa show 1.8 ethanol–ethanol hydrogen bonds per ethanol molecule, which is in fair agreement with previous simulations available in the literature (1.9 at 298 K).<sup>60</sup> The average number of DME–ethanol hydrogen bonds is lower than ethanol–ethanol ones, and lower than 1, decreasing with increasing DME mole fraction with an almost linear trend.

Dynamic properties were also analyzed using molecular dynamics, and thus, self-diffusion coefficients were obtained from mean square displacement and used to calculate the dynamic viscosity using the Stokes–Einstein relationship. Application of the Stokes–Einstein relationship requires the characterization of the hydrodynamic behavior of the studied fluids. As reported in previous sections, the effective hydrodynamic radius for DME is 1.9 Å. Wensink et al.<sup>61</sup> analyzed the dynamic properties of water + alcohol mixtures and showed that the effective hydrodynamic radius for ethanol is 1.85 Å, which is almost the same as the value reported for DME, despite the different sizes of both molecules. Therefore, an effective hydrodynamic radius of 1.9 Å was used to calculate the dynamic viscosity using the Stokes–Einstein equation, in the whole composition range. Calculated self-diffusion coefficients for ethanol and DME are reported in Figure 14a. The simulated  $D$  value for pure ethanol ( $1.10 \times 10^{-9} \text{ m}^2 \text{ s}^{-1}$ ) is slightly larger than the experimental one ( $0.94 \times 10^{-9} \text{ m}^2 \text{ s}^{-1}$ ).<sup>62</sup>  $D$  values for ethanol, which are lower than those for DME, increase with increasing DME mole fraction, which may be justified considering the weakening of ethanol–ethanol hydrogen bonding not compensated for with the new ethanol–DME

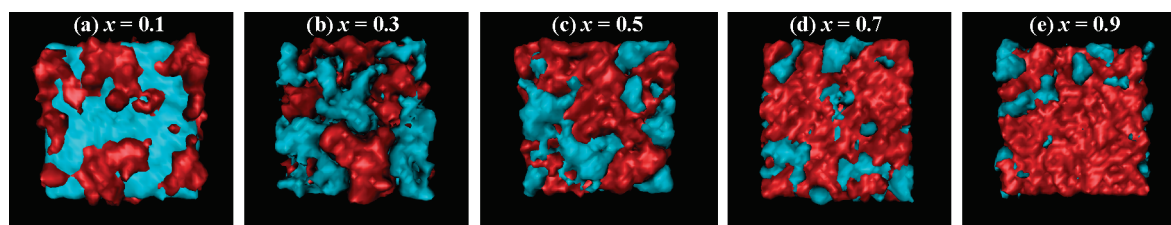


**Figure 15.** Number density maps for DME (red) and ethanol (cyan) in  $x$ DME +  $(1 - x)$ ethanol at 293 K/ $\sim$ 0.1 MPa from NPT molecular dynamics simulations (force field parameters from Tables S1 and S2, Supporting Information). Reported maps are obtained averaging 1 ns simulations and show 10 times the number bulk density for each molecule.

interactions. For DME,  $D$  values increase with increasing DME concentration, with remarkably lower values for low DME mole fractions, which correspond to the larger number of ethanol–DME hydrogen bonds reported in Figure 14. Viscosity values for DME + ethanol mixtures were obtained from mixture  $D$  coefficients calculated from eq 5 and reported in Figure 14b.

$$D = xD_{\text{DME}} + (1 - x)D_{\text{eta}} \quad (5)$$

Simulated dynamic viscosities are lower than experimental values in the whole composition range, although the calculated mixing viscosity reproduces with enough accuracy the experimental behavior.

Finally, we report in Figure 15 the maps of the average number density for ethanol and DME as a function of composition, thus showing the regions of higher DME and ethanol densities. Reported results show the trend of both compounds to cluster with molecules of the same type, thus hindering the development of DME–ethanol heteroassociations through hydrogen bonding. Moreover, in Figure 15a, we show the disrupting effect of DME on ethanol structuring; islands of DME clusters appear, whose size increases with increasing DME mole fraction, thus weakening ethanol–ethanol structuring.

## CONCLUSIONS

The structuring and intermolecular forces in the DME + ethanol binary system were analyzed as a model of the behavior of PEO + ethanol solutions using a collection of computational chemistry tools and several relevant thermophysical properties. The proposed DME force field parametrization leads to low deviations with experimental properties and to a description of DME structuring and conformer distribution in agreement with available literature experimental and computational studies. Computational studies discard the existence of relevant populations of hydrogen-bonded molecules in DME; even for the *tgg'* isomer, this interaction should be very weak. The excess volume and mixing viscosity for DME + ethanol mixtures are negative, which is in agreement with the weakening of intermolecular forces, hydrogen bonding, in ethanol upon mixing with DME, and the relevant role of the available free volumes to fit both molecules in the mixtures. Quantum chemistry results in the gas phase show that DME + ethanol complexes through hydrogen bonding are possible for the five most relevant conformers, leading to moderately strong hydrogen bonds. Molecular dynamics studies confirm the existence of these DME–ethanol hydrogen bonds; nevertheless, the weaker character and extension of these interactions do not balance in an efficient way the disrupting effect of DME on the complex ethanol hydrogen-bonding network. The trend to form microheterogeneities in the

mixed fluid with increasing DME mole fraction is also confirmed through molecular dynamics simulations.

## ASSOCIATED CONTENT

**S Supporting Information.** Force field parameters for 1, 2-dimethoxyethane (Table S1) and ethanol (Table S2), experimental and literature properties for 1,2-dimethoxyethane and ethanol (Table S3), experimental density and dynamic viscosity for DME + ethanol mixtures (Table S4), calculated gas-phase vibrational spectra for the DME–*tgg'* conformer (Figure S1), calculated DME–ethanol complexes in gas phase (Figure S2), and atoms in a molecular analysis of DME–ethanol complexes (Figure S3). This material is available free of charge via the Internet at <http://pubs.acs.org>.

## AUTHOR INFORMATION

### Corresponding Author

\*E-mail: [sapar@ubu.es](mailto:sapar@ubu.es).

## REFERENCES

- (1) Bailey, F. E.; Callard, R. W. *J. Appl. Polym. Sci.* **1959**, *1*, 56.
- (2) Kjellander, R.; Florin, E. *J. Chem. Soc., Faraday Trans.* **1981**, *77*, 2053.
- (3) Zhou, P.; Brown, W. *Macromolecules* **1990**, *23*, 1131.
- (4) Smyth, H. F.; Weil, C. S.; Woodside, M. D.; Knaak, J. B.; Carpenter, C. P. *Toxicol. Appl. Pharmacol.* **1970**, *16*, 442.
- (5) Zgoła-Grześkowiaka, A.; Grześkowiaka, T.; Zembrzuskaa, J.; Łukaszewski, Z. *Chemosphere* **2006**, *64*, 803.
- (6) Dhawan, S.; Dhawan, K.; Varma, M.; Sinha, V. R. *Pharm. Technol.* **2005**, *29*, 72.
- (7) Bruce, P. G.; Scrosati, B.; Tarascon, J. M. *Angew. Chem., Int. Ed.* **2008**, *47*, 2930.
- (8) Bai, H.; Ho, W. S. *J. Membr. Sci.* **2008**, *313*, 75.
- (9) Karan, N. K.; Pradhan, D. K.; Thomas, R.; Natesan, B.; Katiyar, R. S. *Solid State Ionics* **2008**, *179*, 19.
- (10) Devanand, K.; Selser, J. C. *Nature* **1990**, *343*, 739.
- (11) Hammouda, B.; Ho, D. L. *J. Polym. Sci., Part B: Polym. Phys.* **2007**, *45*, 2196.
- (12) Smith, G. D.; Bedrov, D. *Macromolecules* **2002**, *35*, 5712.
- (13) Sturlaugson, A. L.; Fruckey, K. S.; Lynch, S. R.; Atagon, S. R.; Fayer, M. D. *J. Phys. Chem. B* **2010**, *114*, 5350.
- (14) Bedrov, D.; Borodin, O.; Smith, G. D. *J. Phys. Chem. B* **1998**, *102*, 5863.
- (15) Ho, D. L.; Hammouda, B.; Kline, S. R.; Chen, W. *J. Polym. Sci., Part B: Polym. Phys.* **2006**, *44*, 557.
- (16) Hammouda, B. *J. Macromol. Sci., Polym. Rev.* **2010**, *50*, 14.
- (17) Smith, G. D.; Jaffe, R. L.; Yoon, D. Y. *J. Phys. Chem.* **1993**, *97*, 12752.
- (18) Anderson, P. M.; Wilson, M. R. *Mol. Phys.* **2005**, *103*, 89.

- (19) Fischer, J.; Paschek, D.; Geiger, A.; Sadowski, G. *J. Phys. Chem. B* **2008**, *112*, 2388.
- (20) Wagner, W.; Pru, A. *J. Phys. Chem. Ref. Data* **2002**, *31*, 387.
- (21) Lemmon, E. W.; Huber, M. L.; McLinden, M. Reference Fluid and Thermodynamic and Transport Properties. *NIST Standard Reference Database 23*, version 9.0; The National Institute of Standards and Technology: Gaithersburg, MD, 2010.
- (22) Frisch, M. J.; Trucks, G. W.; Schlegel, H. B.; Scuseria, G. E.; Robb, M. A.; Cheeseman, J. R.; Montgomery, Jr., J. A.; Vreven, T.; Kudin, K. N.; Burant, J. C.; Millam, J. M.; Iyengar, S. S.; Tomasi, J.; Barone, V.; Mennucci, B.; Cossi, M.; Scalmani, G.; Rega, N.; Petersson, G. A.; Nakatsuji, H.; Hada, M.; Ehara, M.; Toyota, K.; Fukuda, R.; Hasegawa, J.; Ishida, M.; Nakajima, T.; Honda, Y.; Kitao, O.; Nakai, H.; Klene, M.; Li, X.; Knox, J. E.; Hratchian, H. P.; Cross, J. B.; Adamo, C.; Jaramillo, J.; Gomperts, R.; Stratmann, R. E.; Yazyev, O.; Austin, A. J.; Cammi, R.; Pomelli, C.; Ochterski, J. W.; Ayala, P. Y.; Morokuma, K.; Voth, G. A.; Salvador, P.; Dannenberg, J. J.; Zakrzewski, V. G.; Dapprich, S.; Daniels, A. D.; Strain, M. C.; Farkas, O.; Malick, D. K.; Rabuck, A. D.; Raghavachari, K.; Foresman, J. B.; Ortiz, J. V.; Cui, Q.; Baboul, A. G.; Clifford, S.; Cioslowski, J.; Stefanov, B. B.; Liu, G.; Liashenko, A.; Piskorz, P.; Komaromi, I.; Martin, R. L.; Fox, D. J.; Keith, T.; Al-Laham, M. A.; Peng, C. Y.; Nanayakkara, A.; Challacombe, M.; Gill, P. M. W.; Johnson, B.; Chen, W.; Wong, M. W.; Gonzalez, C.; Pople, J. A. *Gaussian 03*, revision C.02; Gaussian, Inc.: Wallingford, CT, 2004.
- (23) Becke, A. D. *Phys. Rev. A* **1988**, *38*, 3098.
- (24) Lee, C.; Yang, W.; Parr, R. G. *Phys. Rev. B* **1988**, *37*, 785.
- (25) Becke, A. D. *J. Chem. Phys.* **1993**, *98*, 5648.
- (26) Singh, U. C.; Kollman, P. A. *J. Comput. Chem.* **1984**, *5*, 129.
- (27) Besler, B. H.; Merz, K. M.; Kollman, P. A. *J. Comput. Chem.* **1990**, *11*, 431.
- (28) Simon, S.; Duran, M.; Dannenberg, J. J. *Chem. Phys.* **1996**, *105*, 11024.
- (29) Cancès, E.; Mennucci, B. *J. Math. Chem.* **1998**, *23*, 309.
- (30) Bader, R. F. W. *Atoms in Molecules: A Quantum Theory*; Oxford University Press: Oxford, U.K., 1990.
- (31) Biegler-König, F.; Schönbohm, J.; Bayles, D. *J. Comput. Chem.* **2001**, *22*, 545.
- (32) Reed, A. E.; Curtis, L. A.; Weinhold, F. *Chem. Rev.* **1988**, *88*, 899.
- (33) Ponder, J. W. *TINKER: Software Tool for Molecular Design*, 4.2 ed.; Washington University School of Medicine: St. Louis, MO, 2004.
- (34) Hoover, W. G. *Phys. Rev. A* **1985**, *31*, 1695.
- (35) Allen, M. P.; Tildesley, D. J. *Computer Simulation of Liquids*; Clarendon Press: Oxford, U.K., 1989.
- (36) Essmann, U. L.; Perera, M. L.; Berkowitz, T.; Darden, H.; Lee, H.; Pedersen, L. G. *J. Chem. Phys.* **1995**, *103*, 8577.
- (37) Martínez, J. M.; Martínez, L. *J. Comput. Chem.* **2003**, *24*, 819.
- (38) Jorgensen, W. L.; Maxwell, D. S.; Tirado-Rives, J. *J. Am. Chem. Soc.* **1996**, *118*, 11225.
- (39) Hoover, W. G.; Ladd, A. J. C.; Hickman, R. B.; Holian, B. L. *Phys. Rev. A* **1980**, *21*, 1756.
- (40) Haile, J. M. *Molecular Dynamics Simulation: Elementary Methods*; John Wiley and Sons: New York, 1997.
- (41) Cappelezzo, M.; Capellari, C. A.; Pezzin, S. H.; Coelho, A. F. *J. Chem. Phys.* **2007**, *126*, 224516.
- (42) Kuga, S. *J. Chromatogr.* **1981**, *206*, 449.
- (43) Lee, H.; Vries, A. H.; Marrick, S. J.; Pastor, R. W. *J. Phys. Chem. B* **2009**, *113*, 13186.
- (44) Zheng, P.; Meng, X.; Wu, J.; Liu, Z. *Int. J. Thermophys.* **2008**, *29*, 1244.
- (45) Bedrov, D.; Borodin, O.; Smith, G. D.; Trouw, F. *J. Phys. Chem. B* **2000**, *104*, 5151.
- (46) Majer, V.; Svoboda, V. *Enthalpies of Vaporization of Organic Compounds*; Blackwell Scientific Publications: Oxford, U.K., 1985.
- (47) Guevara-Carrion, G.; Nieto-Draghi, C.; Vrabec, J.; Hasse, H. *J. Phys. Chem. B* **2008**, *112*, 16664.
- (48) Yoshida, H.; Tanaka, T.; Matsuura, H. *Chem. Lett.* **1996**, *8*, 637.
- (49) Goutev, N.; Ohno, K.; Matsuura, H. *J. Phys. Chem. B* **2000**, *104*, 9226.
- (50) Yoshida, H.; Kaneko, I.; Matsuura, H.; Ogawa, Y.; Tasumi, M. *Chem. Phys. Lett.* **1992**, *196*, 601.
- (51) Smith, G. D.; Jaffe, R. L.; Yoon, D. Y. *J. Am. Chem. Soc.* **1995**, *117*, 530.
- (52) Koch, U.; Popelier, P. L. A. *J. Phys. Chem.* **1995**, *99*, 9747.
- (53) Popelier, P. L. A. *J. Phys. Chem. A* **1998**, *102*, 1873.
- (54) Yoshida, H.; Matsuura, H. *J. Phys. Chem. A* **1998**, *102*, 2691.
- (55) Linstrom, P. J.; Mallard, W. G., Eds. *NIST Chemistry WebBook, NIST Standard Reference Database Number 69*; The National Institute of Standards and Technology: Gaithersburg, MD, <http://webbook.nist.gov>.
- (56) García, B.; Aparicio, S.; Alcalde, R.; Dávila, M. J.; Leal, J. M. *Ind. Eng. Chem. Res.* **2004**, *43*, 3205.
- (57) Aparicio, S.; Dávila, M. J.; Alcalde, R. *Energy Fuels* **2009**, *23*, 1591.
- (58) Pereira, J. C. G.; Catlow, C. R. A.; Price, G. D. *J. Phys. Chem. A* **2001**, *105*, 1909.
- (59) Aparicio, S.; Alcalde, R. *J. Phys. Chem. B* **2009**, *113*, 14257.
- (60) Saiz, L.; Padró, J. A.; Guàrdia, E. *J. Phys. Chem. B* **1997**, *101*, 78.
- (61) Wensink, E. J. W.; Hoffmann, A. C.; van Maaren, P. J.; van der Spoel, D. *J. Chem. Phys.* **2003**, *119*, 7308.
- (62) Meckl, S.; Zeidler, M. D. *Mol. Phys.* **1988**, *63*, 85.